

LETTER TO THE EDITOR

The uncertain interstellar medium of high-redshift quiescent galaxies: Impact of methodology

R. Gobat¹, C. D'Eugenio^{2,3}, D. Liu⁴, G.B. Caminha^{5,6}, E. Daddi⁷, and D. Blázquez⁸

¹ Instituto de Física, Pontificia Universidad Católica de Valparaíso, Casilla 4059, Valparaíso, Chile

² Instituto de Astrofísica de Canarias (IAC), E-38205 La Laguna, Tenerife, Spain

³ Universidad de La Laguna, Dpto. Astrofísica, E-38206 La Laguna, Tenerife, Spain

⁴ Max-Planck-Institut für extraterrestrische Physik, Gießenbachstraße 1, D-85748 Garching, Germany

⁵ Technische Universität München, Physik-Department, James-Frank Str. 1, 85748 Garching, Germany

⁶ Max-Planck-Institut für Astrophysik, Karl-Schwarzschild-Str. 1, D-85748 Garching, Germany

⁷ CEA, Irfu, DAp, AIM, Université Paris-Saclay, Université de Paris, CNRS, F-91191 Gif-sur-Yvette, France

⁸ DTU-Space, Technical University of Denmark, Elektrovej 327, DK-2800 Kgs. Lyngby, Denmark

ABSTRACT

How much gas and dust is contained in high-redshift quiescent galaxies (QGs) is currently an open question with relatively few and contradictory answers, as well as important implications for our understanding of the nature of star formation quenching processes at cosmic noon. Here we revisit far-infrared (FIR) observations of the REQUIEM-ALMA sample of six $z = 1.6 - 3.2$ QGs strongly lensed by intermediate-redshift galaxy clusters. We measured their continuum emission using priors obtained from high resolution near-infrared (NIR) imaging, as opposed to focusing on point-source extraction, converted it into dust masses using a FIR dust emission model derived from statistical samples of QGs, and compared the results to those of the reference work. We find that, while at least the most massive sample galaxy is indeed dust-poor, the picture is much more nuanced than previously reported. In particular, these more conservative constraints remain consistent with high dust fractions in early QGs. We find that these measurements are very sensitive to the adopted extraction method and conversion factors: the use of an extended light model to fit the FIR emission increases the flux of detections by up to 50% and the upper limit by up to a factor 6. Adding the FIR-to-dust conversion, this amounts to an order of magnitude difference in dust fraction, casting doubts on the power of these data to discriminate between star formation quenching scenarios. Unless these are identified by other means, mapping the dust and gas in high-redshift QGs will continue to require somewhat costly observations.

Key words. Galaxies:early-type – Galaxies:formation – Galaxies:ISM – Gravitational lensing:strong

1. Introduction

In the local Universe, most of the stars are held in so-called quiescent galaxies, which are predominantly spheroidal systems where star formation activity is at very low levels or entirely absent, and which have evolved passively, only becoming older and redder for the past ten billion years. Unsurprisingly, contemporary quiescent galaxies by and large lack the cold gas that fuels star-forming (SF) galaxies such as the Milky Way (e.g., Saintonge et al. 2011; Young et al. 2011; Boselli et al. 2014). Whether they always did, on the other hand, remains an unsolved yet deceptively important question. The stellar component of quiescent galaxies (QGs) has been extensively studied and its evolution traced out to $z \sim 4$, both photometrically (e.g., Davidzon et al. 2017) and spectroscopically (Glazebrook et al. 2017; Schreiber et al. 2018; Tanaka et al. 2019; Valentino et al. 2020). However, the various mechanisms that have been put forward to quench star formation, by either preventing the cooling of gas in and onto galaxies (e.g., Birnboim & Dekel 2003; Croton et al. 2006; Cattaneo et al. 2006), stabilizing it (Martig et al. 2009), or outright expelling it (e.g., Di Matteo et al. 2005; Hopkins et al. 2006), might not leave sufficiently conspicuous signatures in stellar populations. Indeed, galactic archaeology by way of spectroscopic modeling (e.g., Onodera et al. 2015; Gobat et al. 2017; Valentino et al. 2020) has so far

yielded only circumstantial evidence on the quenching pathways of these galaxies (e.g., Onodera et al. 2015; Man & Belli 2018; Pawlik et al. 2019; Belli et al. 2019), constraining the timescale of quenching, but not its specific mechanism. On the other hand, the state of the interstellar medium (ISM) of QGs after quenching should be sensitive to the specific scenario that led to quiescence: for example, a completely expulsive quenching naturally leaves less gas than gravitational stabilization or a mechanism that heats the ISM which, in the latter case, is in a warmer phase (e.g., neutral) on average than if stabilized against fragmentation.

While the gas content of normal, SF galaxies has been extensively traced up to $z \sim 4$ (e.g., Tacconi et al. 2018, 2020; Liu et al. 2019), similar efforts targeting QGs remain sparser and heterogeneous, with CO observations generally placing constraints on their molecular gas fraction (f_{H_2}) ranging from $f_{\text{H}_2} \lesssim 6\%$ upper limits (Sargent et al. 2015; Bezanson et al. 2019; Williams et al. 2021) to $f_{\text{H}_2} = 15 - 25\%$ in some outliers (Rudnick et al. 2017; Hayashi et al. 2018). Interstellar dust, which correlates with total gas (e.g., Magdis et al. 2012), has so far provided the only statistical, though more indirect, constraints on the ISM of QGs for the first five billion years of the history of the Universe. Two approaches based on dust emission have been used which, however, appear to yield contradictory results: the first, using

far-infrared (FIR) spectral energy distributions (SEDs) averaged over large samples, suggests that $z > 1$ QGs retain relatively large amounts of dust and gas (Gobat et al. 2018; Magdis et al. 2021, hereafter, G18 and M21), corresponding to gas fractions of $f_{\text{gas}} \sim 7\%$ at solar metallicity. The data on which these SEDs are based have a variable resolution that is typically lower than the angular size of individual galaxies. They might therefore include contributions from nearby sources, which have to be corrected for. The second approach, on the other hand, involves resolved observations of strongly lensed (and thus magnified) QGs with, however, more limited statistics. Based on these, Whitaker et al. (2021a, hereafter, W21) derived constraints on dust masses which imply significantly lower upper limits of $0.1 - 1\%$ on f_{gas} . However, these conclusions are also based on assumptions, such as the compactness of emission, conversion factors, and (in particular, since the observations only sample the Rayleigh-Jeans tail of dust emission) dust temperature. It is therefore not immediately clear whether the apparent tension between these two types of constraints is not simply an artifact of mismatched assumptions.

To remedy this doubt, we revisited the lensed QG sample of W21 using a methodology consistent with that of G18 and M21. Section 2 briefly summarizes the sample and data, Sect. 3 describes our analysis, Sect. 4 provides the results, and Sect. 5 presents our conclusions. We assumed a concordance cosmology with $H_0 = 70 \text{ km s}^{-1} \text{ Mpc}^{-1}$, $\Omega_M = 0.3$, and $\Omega_\Lambda = 0.7$, as well as a Salpeter (1955) initial mass function (IMF), with quantities from the literature having been converted to this IMF.

2. Sample and data

The REQUIEM-ALMA sample (W21) consists of six QGs at $z = 1.5 - 3.2$ observed under programs 2018.1.00276 (PI K.E. Whitaker) and 2019.1.00227 (PI J. Tan) with the Atacama Large Millimeter/Submillimeter Array (ALMA) at 1.3 mm , corresponding to the ALMA Band 6 and $300 - 500 \mu\text{m}$ rest frame. We obtained the raw data from the ALMA Science Archive and processed them to produce calibrated visibility sets, which were then split and binned in both time and channels, and finally exported as a single continuum UVFITS table per QG with GILDAS¹. All six QGs are strongly lensed by intermediate-redshift ($z = 0.3 - 0.8$) massive galaxy clusters, with two creating giant arc images. Due to the nature of the lenses, they benefit from optical-near-infrared (NIR) imaging by the Hubble (HST) and *Spitzer* space telescopes, accumulated over the years under a variety of observing programs and publicly available in their respective archives. Table A.1 summarizes the photometric coverage of these fields. The lensed galaxies themselves have also been observed spectroscopically, with them and the data being described in Newman et al. (2018, hereafter, N18) and Man et al. (2021). We refer the reader to these articles for more information and we adopt their naming conventions throughout.

3. Analysis

Based on two point-like detections, W21 concluded that the 1.3 mm emission from dust was confined to compact, unresolved regions of the QGs. These correspond, spatially, to their cores (the central kiloparsec, in the case of the most extended, MRG-0138), which are also the brightest regions of the galaxies in stellar light. More recently, the QG MRG-2129 was followed

up on with ALMA at very high resolution by Morishita et al. (2022), who similarly concluded that the emission is compact and localized. However, this new observation consists of a single pointing with a maximum recoverable scale of $\sim 0.6''$, or half the beam width of the data used in W21. Therefore, if conversely the distribution of dust includes an overall continuous component following the stellar one, the emission from lower-surface brightness regions could very well be either below the noise level of the data or missed entirely by the instrument. As a test, we examined resolved, integral field spectroscopy of two of the most extended galaxies in the sample, MRG-0138 and MRG-1341 (see Appendix B). Within the wavelength range of the spectra, we found no appreciable difference between the bright central regions of these galaxies and their extended outer regions, which would for example suggest that one contains a larger fraction of younger stars than the former.

For each galaxy, we first constructed a model of their stellar distribution from the longest-wavelength high-resolution data available, namely the HST Wide Field Camera 3 (WFC3) F160W imaging, corresponding to the rest-frame optical range. Cutouts centered on the QGs were extracted from the F160W images and the light of nearby objects was modeled and subtracted using GALFIT (Peng et al. 2010). All pixels below 3σ of the background value were then zeroed out, using SExtractor (Bertin & Arnouts 1996) on the residual image to isolate the QG. We note that, while this threshold was chosen to avoid including image noise in the model, it might cut out some of the galaxies' extended profiles. However, as the F160W data are deep compared to the brightness of the lensed QGs, the loss of emission should not be significant. The use of these stellar light models should therefore come closest to reproducing the effective aperture of the SED stacks in M21, minus the potential residual contamination by nearby sources. The cutout images and resulting models are shown in Fig. 1 (top and second row, respectively).

To account for astrometry differences between the F160W and ALMA data, the fit allowed for a free offset. For detected objects, this yielded offsets of $< 0.15''$, which is significantly smaller than the spatial resolution of the ALMA data. Any bright sources present in the field of view (MRG-0454 and MRG-1341) were modeled at the same time, so as to mitigate the possibility of contamination from sidelobes. In cases where the residuals of the extended model fit contained noticeable ($> 3\sigma$) leftover emission, we also allowed for excess central emission in the form of an additional point source with free amplitude for a total of two components per fit in this case. One exception was MRG-0138, where the lensed arc targeted by the ALMA observation is a combination of two images bisected by a critical line. We did not attempt to separate them, but rather counted them as a single image, thus requiring the use of two point-source components, with relative amplitudes fixed by the ratio of mean magnifications between the two images given in N18. We then corrected the quantities derived for this object to the magnification factor of the first image (N18). As a sanity check and to allow for a direct comparison with W21, we also extracted 1.3 mm fluxes by fitting a point source without the total light model. Uncertainties (and thus upper limits) for model and point source fluxes were estimated from the r.m.s. dispersion of a thousand extractions performed with each component at random positions with large offsets from phase center (that is, staying well clear of the target galaxy and other sources within the field of view). The resulting mag-

¹ <http://www.iram.fr/IRAMFR/GILDAS>

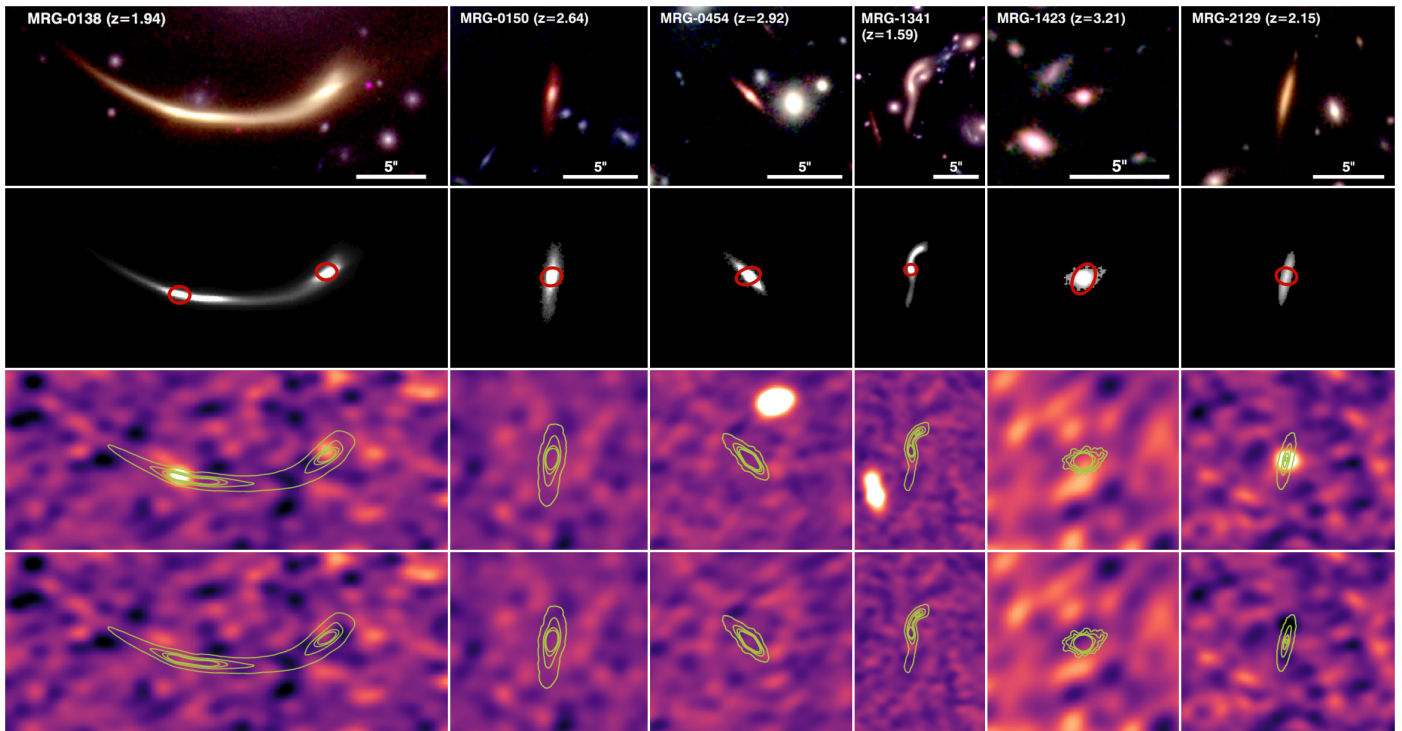


Fig. 1. Cutouts of the six lensed QGs reanalyzed in this work. The rows, from top to bottom, show: color images (HST F160W, F140W, or F125W, and F105W) with scale bar; stellar light models with the ALMA synthesized beam shown as a red ellipse; and ALMA Band 6 continuum images and residuals after subtraction of the model, with the $1.6\,\mu\text{m}$ light distribution shown as green contours.

nified fluxes and errors, or 3σ upper limits, are shown in Table 1.

3.1. Dust masses

We then converted these fluxes into (magnified) dust masses using the average FIR SED template for $z > 0$ QGs of M21, sampled at 1.3 mm. This model has a dust temperature of $T_d = 21\,\text{K}$, which is a few Kelvin lower than the mass-weighted T_d typically used for SF galaxies (Scoville et al. 2016, 2017, hereafter S16). In addition to being consistent with the methodology of M21, with which we compare in this study, we consider it a more likely description of the ISM of QGs which, given their quiescence, should be subjected to a softer radiation field than in SF galaxies. If the FIR SEDs used in M21 were contaminated by, for example, SF occurring at a similar redshift (i.e., from satellite galaxies), the true T_d of high-redshift QGs might be even lower. To summarize, here, we consider three analysis methods. In order of complexity, they are as follows: point-source extraction converted to a dust mass using S16, point-source extraction converted to dust mass using the M21 SED, and an extended model fit converted to dust using M21. For clarity, we do not include the fourth possible combination here, that is, the extended model fit with the S16 calibration, as it falls between the first and third method and can be easily inferred from the first three (see Sect. 4). The dust masses or upper limits corresponding to both model+point and point-source fluxes are given in Table 1.

3.2. Stellar masses

For consistency with the ALMA analysis, we also recomputed stellar masses for the six REQUIEM-ALMA QGs from SEDs

based on the F160W light model used to fit the ALMA data. That is, we extracted photometry from HST images using SEXTRACTOR in dual-image mode, with the F160W model as a reference. For *Spitzer* data, which have significantly lower resolution and are thus often blended, we instead performed a multicomponent decomposition² of the image, using the F160W model and GALFIT models of nearby objects convolved with the point response functions of *Spitzer*/IRAC. We then modeled these SEDs with Bruzual & Charlot (2003) stellar population templates, assuming star formation histories (SFHs) with exponential cutoffs, as already used for high-redshift QGs (e.g., Schreiber et al. 2018; Valentino et al. 2020). We checked that the stellar masses thusly obtained are consistent with those from the literature. We refer the reader to Appendix D for more details.

4. Results

Of the two point-like detections in W21, the emission of MRG-2129 is well-fitted by the extended stellar light model (Fig. 1, right) without compact emission, with slightly lower residuals than when using a point source; although, the difference is not significant. With the same conversion factor, this yields a 50% larger M_d than when only considering compact emission (W21, Morishita et al. 2022). On the other hand, MRG-0138 requires an additional point-like component, accounting for $\sim 45\%$ of the total flux per image. For this object, the error on the flux is thus taken as the quadrature sum of model and point-source uncertainties. The other four galaxies in the sample remain undetected at the 3σ level, in which case we only considered uncertainties from the stellar light model.

² with MPFIT (Markwardt 2009)

Table 1. Lensed galaxy properties

| ID | z | $\log \mu M_\star$ | $\mu f_{1.3\text{mm,model}}$ | $\mu f_{1.3\text{mm,point}}$ | $\log \mu M_{d,\text{model}}$ | $\log \mu M_{d,\text{point}}$ | μ |
|------|---------------------|-------------------------|------------------------------|------------------------------|-------------------------------|-------------------------------|------------------|
| | | M_\odot | μJy | μJy | M_\odot | M_\odot | |
| 0138 | 1.9439 ^a | $13.05^{+0.14}_{-0.10}$ | 352 ± 116 | 285 ± 29 | 9.11 ± 0.15 | 9.02 ± 0.04 | 12.5 ± 5.4^a |
| 0150 | 2.6355 ^a | $12.24^{+0.25}_{-0.19}$ | < 180 | < 52 | < 9.30 | < 8.76 | 4.4 ± 1.1^a |
| 0454 | 2.9225 ^b | $11.72^{+0.13}_{-0.09}$ | < 174 | < 42 | < 8.81 | < 8.19 | 10.9 ± 2.1^b |
| 1341 | 1.5943 ^b | $12.20^{+0.14}_{-0.12}$ | < 161 | < 27 | < 8.76 | < 7.98 | 30 ± 8^b |
| 1423 | 3.2092 ^b | $11.27^{+0.21}_{-0.07}$ | < 91 | 28 ± 11 | < 8.52 | 8.01 ± 0.17 | 2.7 ± 2^b |
| 2129 | 2.1487 ^a | $11.88^{+0.14}_{-0.08}$ | 247 ± 66 | 164 ± 17 | 8.96 ± 0.12 | 8.78 ± 0.05 | 4.6 ± 0.2^b |

^aNewman et al. (2018), ^bMan et al. (2021)

Under the assumption that interstellar dust and stars have comparable distributions in the source plane, the dust-to-stellar mass ratio M_d/M_\star does not depend on the lensing magnification μ . We note that, in any other case, correctly estimating M_d/M_\star would require the usage of a full lensing model to account for differential magnification across images. We therefore do not include the uncertainty on μ in the formal error on this ratio. Likewise, here, we focus our discussion on dust fractions, so as to not depend on the uncertain dust-to-gas conversion factor (92 for M21, 100 for W21). Fig. 2 shows the M_d/M_\star of the REQUIEM-ALMA galaxies, as a function of redshift and stellar mass, for the three different flux extraction and 1.3 mm-to-dust conversion cases: point sources with the S16 calibration, as in W21; point sources with the M21 SED; and extended models with the M21 SED. For comparison, we also include in Fig. 2 literature constraints on the M_d/M_\star of S0851, which is another lensed QG (though unresolved in the FIR) discussed in Caliendo et al. (2021). The first case yields the lowest M_d/M_\star , while the second one produces values higher by a factor 3 – 3.5. As noted in M21, the difference between these two estimates stems from the higher T_d used by S16, which implies a higher dust luminosity per unit mass. Using the extended emission model (third case) raises M_d/M_\star by another 25%-50% for detected objects and a factor 3-5 in the case of upper limits, depending on the size of the galaxy.

Using the stellar light model and M21 SED, the constraints on the M_d/M_\star of the REQUIEM-ALMA galaxies become consistent with those derived from FIR SEDs (G18, M21) and thus with a scenario where relatively young QGs retain a non-negligible ISM, as found by Suess et al. (2017) and Bezanson et al. (2022) at intermediate redshift. However, we caution that, while at least one object (MRG-2129) has 0.13% dust, implying $f_{\text{gas}} \sim 10\%$, the upper limits derived here remain compatible with much lower ISM fractions, which makes it difficult to draw firm conclusions on quenching scenarios from these data.

The notable exception is MRG-0138 which, even in this new analysis, remains almost an order of magnitude more dust-poor than the other five QGs. Assuming no systematic error in its estimated magnification, it is also the most massive galaxy in the sample, occupying the high-mass tip of the galaxy mass function in its redshift range (e.g., Davidzon et al. 2017), and it is possibly the oldest when accounting for differences in redshift (N18 and Appendix B). This suggests a host dark matter halo with a mass $> 5 \times 10^{13} M_\odot$ (at 3σ , assuming parameter and M_\star

uncertainties as well as the $M_\star - M_{\text{halo}}$ relation of Girelli et al. 2020), where cold gas accretion should have become inefficient at $z \gtrsim 3$ (Dekel & Birnboim 2006), around which time quenching likely began. Since dust is destroyed over time in QGs (e.g., Smercina et al. 2018; Whitaker et al. 2021b), its low concentration in MRG-0138 is therefore unsurprising. For example, a depletion time for dust of ~ 1.7 Gyr (Michałowski et al. 2019; Gobat et al. 2020) would imply that the initial dust mass after quenching was higher by at least a factor 2. This mirrors the anticorrelation between f_{gas} and stellar mass seen in the local Universe (e.g., Young et al. 2011; Saintonge et al. 2017; Tacconi et al. 2018, 2020; Liu et al. 2019; Saintonge & Catinella 2022).

5. Conclusions

In this Letter, we revisited the REQUIEM-ALMA literature sample of six lensed QGs. We analyzed the ALMA Band 6 continuum observations of these galaxies, described in W21, with a different methodology and assumptions. Namely, we allowed for extended dust emission coterminous with the stellar distribution, with or without an additional compact component, and we converted the measured intensities to dust masses using an empirical FIR SED derived from larger statistical QG samples. We found that, while some tension with SED-derived results might still exist, the method used for FIR flux extraction and the light-to-mass conversion factor both have a significant impact on the estimate of their dust fractions, with both adding up to an order of magnitude variation. In particular, opting for extended models based on the stellar surface brightness of the targets has the effect of relaxing, if not eliminating, said tension. Under our physically motivated assumptions, the constraints on the dust fraction of this sample are broadly consistent with the $M_d/M_\star \sim 0.08 - 0.09\%$ values derived by G18 and M21 for coeval QGs from lower-resolution FIR stacks.

On the other hand, we confirm the scant dust content of MRG-0138 determined in W21. This object, being the most massive member of the sample, has likely experienced the most biased evolution. Its tension with the stacked results of G18 and M21 might then be explained by an anticorrelation between ISM mass and stellar mass being already present at this epoch, which would be largely diluted with them being averaged over large samples with relatively broad stellar mass ranges.

Knowing whether the ISM of high-redshift QGs is confined to central cores, distributed but clumpy, or diffuse would drive the choice of the extraction method. Simulations could in princi-

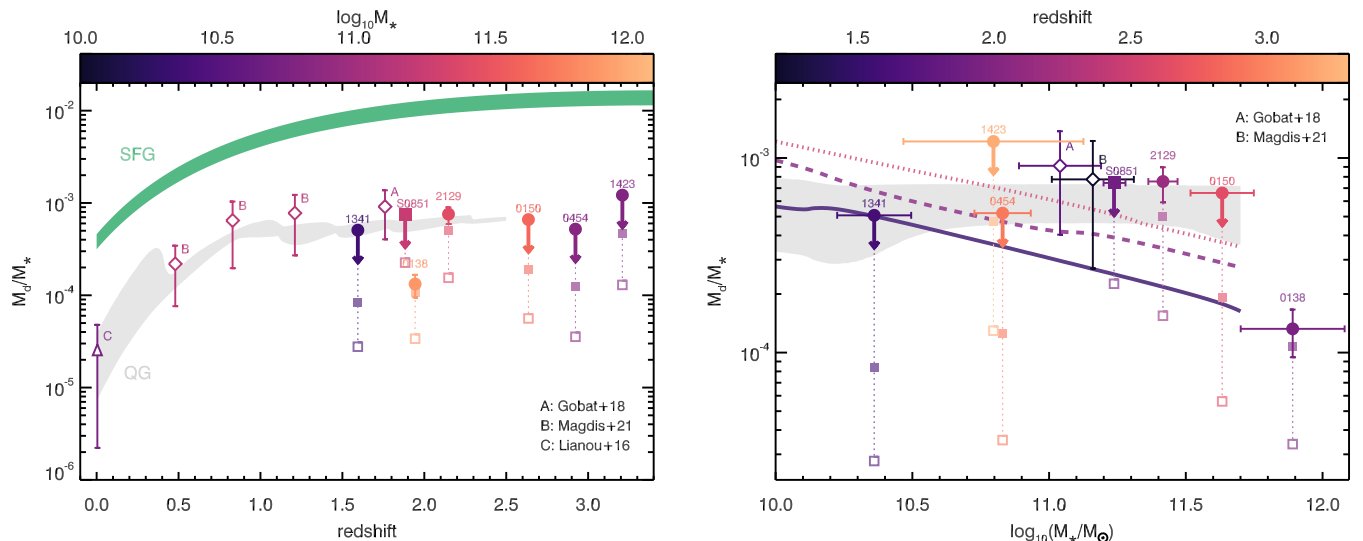


Fig. 2. Dust-to-stellar mass fraction of lensed QGs (W21; Caliendo et al. 2021) as a function of redshift (left) and stellar mass (right), compared to stacked samples (G18 and M21) and local QGs (Lianou et al. 2016). Filled dots show the constraints derived from extended model fits, while open and filled squares correspond to point-source fluxes converted to dust masses using the S16 parameterization and M21 templates, respectively. All symbols are color-coded as a function of either stellar mass (left panel) or redshift (right panel). The right panel also shows the expected average dust fraction of QGs, from a simple model based on the evolution of their mass function (Gobat et al. 2020), assuming that either the initial dust fraction after quenching is a fixed fraction of the main sequence one (solid, dashed, and dotted lines corresponding to $z = 1.5$, 2, and 2.5, respectively) or constant irrespective of redshift and mass (gray envelope, for the same redshift range). In the left panel, the green curve shows the typical dust fraction of main sequence galaxies (Whitaker et al. 2014), while the gray envelope corresponds to the redshift evolution of the Gobat et al. (2020) model.

ple inform us on the likely true amount and distribution of dust and gas in early QGs, if sufficiently well bracketed by other observables. On the other hand, the current statistics allowed by strong lensing, and the data thereon at their current depth, are not sufficient to draw definitive conclusions on this aspect. Given the current lack of consensus regarding the total ISM mass of these galaxies, resolved observations thus need to be taken with caution.

Acknowledgements. GBC acknowledges the Max Planck Society for financial support through the Max Planck Research Group for S.H.Suyu and the academic support from the German Centre for Cosmological Lensing.

References

- Belli, S., Newman, A.B., Ellis, R.S. 2019, *ApJ*, 874, 17
 Bertin, E. & Arnouts, S. 1996, *A&AS*, 117, 393
 Bezanson, R., Spilker, J., Williams, C. et al. 2019, *ApJ*, 873, 19
 Bezanson, R., Spilker, J., Suess, K.A. et al. 2022, *ApJ*, 925, 153
 Birnboim, Y. & Dekel, A. 2003, *MNRAS*, 345, 349
 Boselli, A., Cortese, L., Boquien, M. et al. 2014, *A&A*, 564, A66
 Bruzual, G. & Charlot, S. 2003, *MNRAS*, 344, 1000
 Caliendo, J.N., Whitaker, K.E., Akhshik, M. et al. 2021, *ApJ*, 910, 7
 Cattaneo, A., Dekel, A., Devriendt, J., Guiderdoni, B., Blaizot, J. 2006, *MNRAS*, 370, 1651
 Croton, D.J., Springel, V., White, S.D.M. et al. 2006, *MNRAS*, 365, 11
 Davidzon, I., Ilbert, O., Laigle, C. et al. 2017, *A&A*, 605, A70
 Dekel, A. & Birnboim, Y. 2009, *MNRAS*, 368, 2
 Di Matteo, T., Springel, V., Hernquist, L. 2005, *Nature*, 433, 604
 Fanelli, M.N., O'Connell, R.W., Burstein, D., Wu, C. 1992, *ApJS*, 82, 197
 Girelli, G., Pozzetti, L., Bolzonella, M. et al. 2020, *A&A*, 634, A135
 Glazebrook, K., Schreiber, C., Labbé, I. et al. 2017, *Nature*, 544, 71
 Gobat, R., Daddi, E., Strazzullo, V. et al. 2017, *A&A*, 599, A95
 Gobat, R., Daddi, E., Magdis, G. et al. 2018, *Nature Astronomy*, 2, 239
 Gobat, R., Magdis, G., D'Eugenio, C., Valentino, F. 2020, *A&A*, 644, L7
 Hayashi, M., Tadaki, K., Kodama, T. et al. 2018, *ApJ*, 856, 118
 Hopkins, P.F., Somerville, R.S., Hernquist, L. et al. 2006, *ApJ*, 652, 864
 Lianou, S., Xilouris, E., Madden, S.C., Barnby, P. 2016, *MNRAS*, 461, 2856
 Liu, D., Schinnerer, E., Groves, B. et al. 2019, *ApJ*, 887, 235
 Magdis, G., Daddi, E., Béthermin, M. et al. 2012, *ApJ*, 760, 6
 Magdis, G., Gobat, R., Valentino, F. et al. 2021, *A&A*, 647, A33
 Man, A.W.S. & Belli, S. 2018, *Nature Astronomy*, 2, 695
 Man, A.W.S., Zabl, J., Brammer, G. et al. 2021, *ApJ*, 919, 20
 Maraston, C., Nieves Colmenáez, L., Bender, R., Thomas, D. 2009, *A&A*, 493, 425
 Markwardt, C.B., 2009, *ASPC*, 411, 251
 Martig, M., Bournaud, F., Teyssier, R., Dekel, A. 2009, *ApJ*, 707, 250
 Michałowski, M.J., Hjorth, J., Gall, C. et al. 2019, *A&A*, 632, 43
 Morishita, T., Abdurro'uf, Hirashita, H. et al., arXiv:2208.10525
 Newman, A.B., Belli, S., Ellis, R.S., Patel, S.G. 2018, *ApJ*, 862, 125
 Onodera, M., Carollo, C.M., Renzini, A. et al. 2015, *ApJ*, 808, 161
 Pawlik, M.M., McAlpine, S., Trayford, J.W. et al. 2019, *Nature Astronomy*, 3, 440
 Peng, C.Y., Ho, L.C., Impey, C.D., Rix, H.-W. 2010, *AJ*, 139, 2097
 Rudnick, G., Hodge, J., Walter, F. et al. 2017, *ApJ*, 849, 27
 Saintonge, A., Kauffmann, G., Kramer, C. et al. 2011, *MNRAS*, 415, 32
 Saintonge, A., Catinella, B., Tacconi, L.J. et al. 2017, *ApJS*, 233, 22
 Saintonge, A. & Catinella, B. 2022, *ARA&A*, 60, 319
 Salpeter, E.E. 1955, *ApJ*, 121, 161
 Sargent, M.T., Daddi, E., Bournaud, F. et al. 2015, *ApJ*, 806, 20
 Schreiber, C., Glazebrook, K., Nanayakkara, T. et al. 2018, *A&A*, 618, A85
 Scoville, N., Sheth, K., Aussel, H. et al. 2016, *ApJ*, 820, 83
 Scoville, N., Lee, N., Vanden Bout, P. et al. 2017, *ApJ*, 837, 150
 Smercina, A., Smith, J.D.T., Dale, D.A. et al. 2018, *ApJ*, 855, 51
 Soto, K.T., Lilly, S.J., Bacon, R. et al. 2016, *MNRAS*, 458, 3210
 Suess, K.A., Bezanson, R., Spilker, J.S. et al. 2017, *ApJ*, 846, 14
 Tacconi, L.J., Genzel, R., Saintonge, A. et al. 2018, *ApJ*, 853, 179
 Tacconi, L.J., Genzel, R., Sternberg, A. 2020, *ARA&A*, 58, 157
 Tanaka, M., Valentino, F., Toft, S. et al. 2019, *ApJ*, 885, 34
 Valentino, F., Tanaka, M., Davidzon, I. et al. 2020, *ApJ*, 889, 93
 Vazdekis, A., Sánchez-Blázquez, P., Falcón-Barroso, J. et al. 2010, *MNRAS*, 404, 1639
 Weibacher P.M., Palsa, R., Streicher, O. et al. 2020, *A&A*, 641, A28
 Whitaker, K.E., Franx, M., Leja, J. et al. 2014, *ApJ*, 795, 104
 Whitaker, K.E., Williams, C.C., Mowla, L. et al. 2021, *Nature*, 597, 485
 Whitaker, K.E., Narayanan, D., Williams, C.C. et al. 2021, *ApJ*, 922, 30
 Williams, C.C., Spilker, J.S., Whitaker, K.E. et al. 2021, *ApJ*, 908, 54
 Young, L.M., Bureau, M., Davis, T.A. et al. 2011, *MNRAS*, 414, 940

Appendix A: HST and Spitzer coverage

Table A.1 shows the broadband photometric coverage by the HST and *Spitzer* telescopes of the fields of each QG, with each dot indicating that public imaging data are available from their respective archives.

Table A.1. Broadband photometric coverage

| Band | MRG- | | | | | |
|--------|------|------|------|------|------|------|
| | 0138 | 0150 | 0454 | 1341 | 1423 | 2129 |
| F275W | | | | | • | |
| F336W | | | | | • | • |
| F390W | • | | | | • | • |
| F435W | | | | | • | • |
| F475W | | | | | • | • |
| F555W | • | | • | | • | • |
| F606W | | • | | • | • | • |
| F625W | | | | | | • |
| F775W | | | • | | • | • |
| F814W | • | • | • | • | • | • |
| F850LP | | | • | | • | • |
| F105W | • | • | • | • | • | • |
| F110W | • | • | • | • | • | • |
| F125W | • | • | • | • | • | • |
| F140W | • | • | • | • | • | • |
| F160W | • | • | • | • | • | • |
| IRAC1 | • | • | • | • | • | • |
| IRAC2 | | • | • | • | • | • |
| IRAC3 | | | • | | • | • |
| IRAC4 | | | • | | • | • |

Appendix B: Spatially resolved spectroscopy

We obtained integral field spectroscopic data of two of the six targets from the Science Archive of the European Southern Observatory (ESO). The clusters MACS0138 and MACS1341 were observed with the Multi Unit Spectroscopic Explorer (MUSE) on the Very Large Telescope (VLT) under ESO programs 0103.A-0777 (PI A. Edge) and 0103.B-0717 (PI A. Man), respectively. MACS0138 was observed for a total of 48.5 minutes on target with a median seeing of $\sim 0.8''$, while MACS1341 was observed for a total of 82 minutes using the Ground Layer Adaptive Optics (GLAO) system, which provided a final point spread function (PSF) width of $0.55''$ measured from the white light image (i.e., the data cube collapsed along its wavelength axis). The raw data were reduced using the standard MUSE pipeline (version 2.8; Weilbacher et al. 2020) to produce corrected and calibrated data cubes. We then applied the *Zurich Atmosphere Purge* tool (ZAP; Soto et al. 2016) to improve the sky subtraction and, for each cluster, matched the world coordinate system (WCS) of the data cube (based on the white image) to that of the HST/WFC3 F160W image. Further details on the data and their reduction will be given in Caminha et al. (in prep.).

We divided each of the F160W stellar light models into two areas of equal total flux, corresponding to an inner (or “bulge”) and outer (or “disk”) region. We then rebinned these masks to the MUSE pixel size and produced a median stacked 1D spectrum for each. We computed an associated noise spectrum using the

jackknife method as

$$\sigma = \sqrt{\frac{N-1}{N} \sum_{i=1}^N (f - f_i)^2}, \quad (\text{B.1})$$

where N is the number of pixels, f_i the spectrum corresponding to the i -th pixel, and f the coadded spectrum.

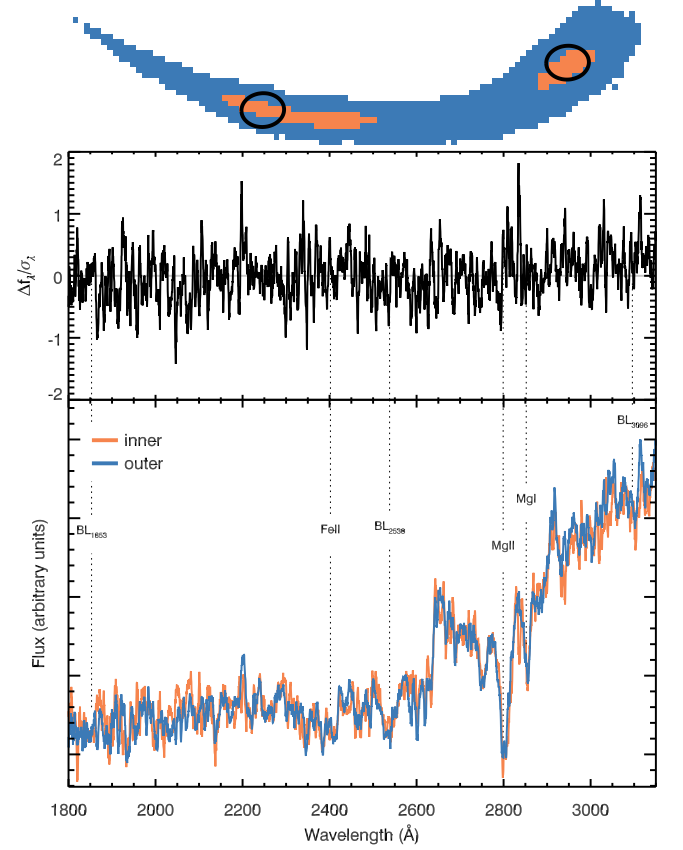


Fig. B.1. *Bottom panel:* Average VLT/MUSE spectra of inner (orange) and outer (blue) regions in the MRG-0138 arc image, covering the 1800 – 3150 Å rest-frame wavelength range and smoothed with a ten-pixel kernel for clarity. Significant near-ultraviolet features are indicated by dotted lines. *Middle panel:* Signal-to-noise ratio of the difference spectrum (inner – outer) as a function of wavelength. *Top panel:* Mask of the MRG-0138 arc showing inner (orange) and outer (blue) regions, with the corresponding ALMA band 6 beams shown as black ellipses.

Figs. B.1 and B.2 compare the inner and outer VLT/MUSE spectra of MRG-0138 and MRG-1341, respectively, with the signal-difference-to-noise spectrum shown in the middle panel. In both cases, we find no appreciable difference between spectral features within the two regions. Spectral modeling based on the parametric SFH described in Appendix D produces consistent mass-weighted ages of ~ 1.5 Gyr and ~ 1.8 Gyr. Similarly, adopting a nonparametric fit with Vazdekis et al. (2010) templates, as done in Gobat et al. (2017), yield very similar age and metallicity distributions, within uncertainties. However, we caution that, although the absorption features covered by the MUSE spectra correlate with a combination of age and metallicity (Fanelli et al. 1992; Maraston et al. 2009), being limited to the near-ultraviolet, which is most sensitive to young massive stars, makes them suboptimal for reconstituting SFHs. In

addition, some stellar populations could be invisible if, for example, they are entirely shrouded by dust. Alternatively, a signal of inside-out or outside-in quenching might still be present, but more subtle than what these particular data can resolve. Finally, we note that these results do not change if mean spectra are used or if we define the inner region using the ALMA beam (see top panels in Figs. B.1 and B.2) rather than isophotes.

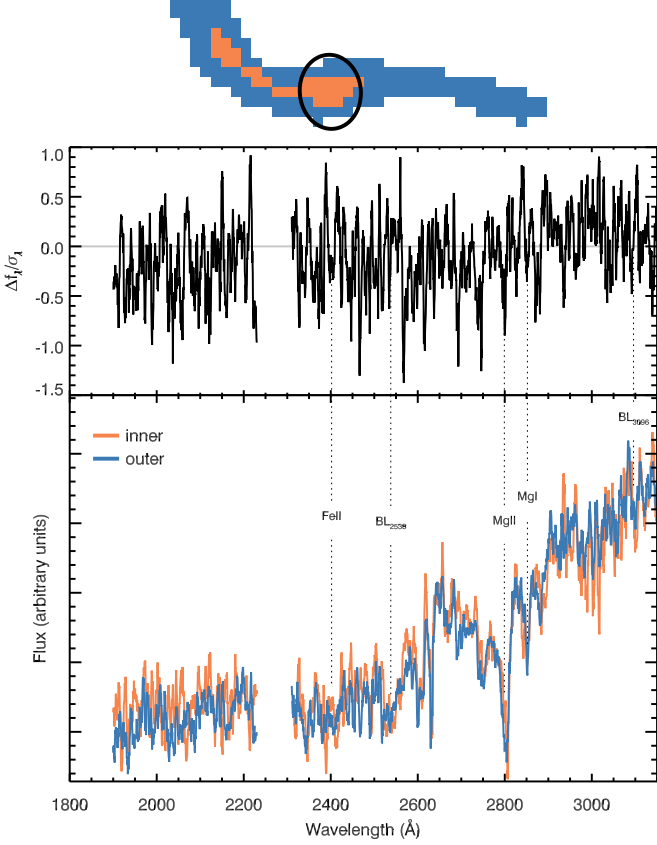


Fig. B.2. Same as Fig. B.1, but for MRG-1341.

Appendix C: uv plane modeling

Given an intensity distribution on the sky of $M(x, y)$, where x and y are spatial coordinates from the phase center, we modeled the complex visibility as

$$V(u, v) = \iint B(x, y) M(x, y) e^{2\pi i(ux+vy)} dx dy, \quad (\text{C.1})$$

where $B(x, y) = (2J_1(\theta)/\theta)^2$ is the primary beam response of the antennas, with J_1 the first order Bessel J function, $\theta = \sqrt{x^2 + y^2}/\text{HWBN}$, and HWBN is the half-beam width at first null. Here we assumed that there are no significant differences in astrometry between the ALMA and HST data. In cases where a bright off-center source exists in the field of view (e.g., for MRG-1341; see Fig. 1), this appears to be the case.

Appendix D: Comparison of stellar masses

Fig. D.1 compares previously published stellar masses of the QG sample with those used in this work. The latter masses were es-

timated from fits to their HST and *Spitzer* SEDs, extracted using SExtractor (Bertin & Arnouts 1996) in dual-image mode with the HST/WFC3 F160W model as the base, using Bruzual & Charlot (2003) stellar population models. We assumed metallicity priors from spectroscopy (Newman et al. 2018; Man et al. 2021) and delayed exponentially declining SFHs with an exponential cutoff of the form

$$\text{SFR}(t) \propto \frac{t}{\tau^2} e^{-t/\tau} \min(e^{-(t-t_q)/\tau_q}, 1) \quad (\text{D.1})$$

(where t is the time since the beginning of star formation, τ the SFH's e -folding timescale, and t_q and τ_q parameterize the start and timescale of quenching, respectively), which is appropriate for high-redshift QGs (e.g., Schreiber et al. 2018; Valentino et al. 2020). Here we fixed the start of the SFH at $z = 10$ and assumed parameter ranges of (0, 3] Gyr for τ , [1, 3] Gyr for t_q , and [0.1, 1.] Gyr for τ_q .

The stellar masses thusly derived from the SEDs are consistent with those published in previous works and used in W21, except for MRG-1341, where our estimate is almost a factor 2 higher. As a consequence, the M_d/M_* of MRG-1341 presented in this Letter is lower by half than if we had used the literature value.

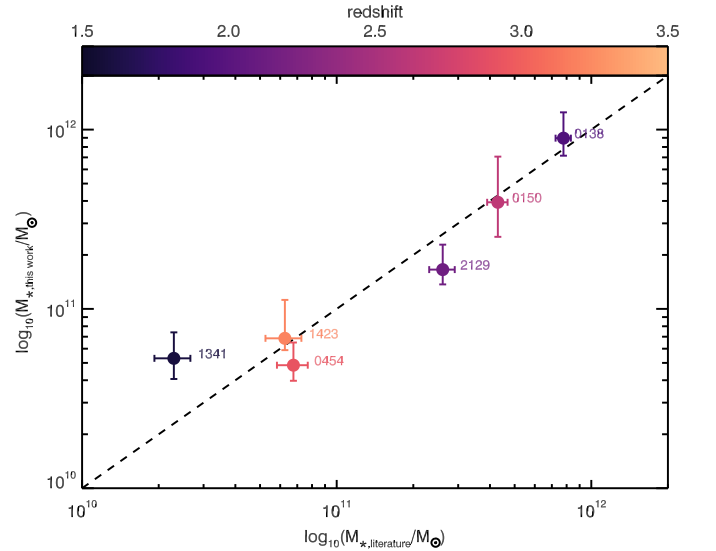


Fig. D.1. Comparison between stellar masses of the REQUIEM-ALMA sample reported in previous works (Newman et al. 2018; Man et al. 2021) and computed here from HST+*Spitzer* SEDs with metallicity priors. The masses from the literature were converted to a Salpeter (1955) IMF and both have been de-magnified; however, the error bars shown here do not account for magnification uncertainties. The dashed line shows the one-to-one relation.